1   **Structural basis for late maturation steps of the human mitoribosomal large subunit**

2

3

4   **Authors:** Miriam Cipullo[1,2,†], Genís Valentín Gesé[3,†], Anas Khawaja[1,2],

5   B. Martin Hällberg[3,4,*], Joanna Rorbach[1,2,*]

6

7

8   **Affiliations:**

9   [1] Department of Medical Biochemistry and Biophysics, Division of Molecular Metabolism,

10   Karolinska Institutet, Solnavägen 9, 171 65 Solna, Sweden

11   [2] Max Planck Institute Biology of Ageing - Karolinska Institutet Laboratory, Karolinska

12   Institutet, Stockholm, Sweden

13   [3] Department of Cell and Molecular Biology, Karolinska Institutet, Solnavägen 9, 171 65

14   Solna, Sweden

15   [4] Centre for Structural Systems Biology (CSSB) and Karolinska Institutet VR-RÅC,

16   Notkestrasse 85, 22607 Hamburg, Germany.

17

18

19   †Joint First Authors

20

21   *Correspondence to:

22   B. Martin Hällberg

23   Address: Department of Cell and Molecular Biology, Karolinska Institutet, Solnavägen 9, 171

24   65 Solna, Sweden

25   Email: martin.hallberg@ki.se

26

27   Joanna Rorbach

28   Department of Medical Biochemistry and Biophysics, Research Division of Molecular

29   Metabolism, Karolinska Institutet, Solnavägen 9, 171 65 Solna, Sweden

30   Email: joanna.rorbach@ki.se

31

32

33

34

Abstract

Mitochondrial ribosomes (mitoribosomes) synthezise a critical set of proteins essential for oxidative phosphorylation. Therefore, their function is vital to cellular energy supply and mitoribosomal defects give rise to a large and diverse group of human diseases [1]. The architecture of mitoribosomes is strikingly different from that of their bacterial and eukaryotic cytosolic counterparts and display high divergence between species [2–6]. Mitoribosome biogenesis follows distinct molecular pathways that remain poorly understood. Here, we determined the cryo-EM structures of mitoribosomes isolated from human cell lines with either depleted or overexpressed mitoribosome assembly factor GTPBP5. This allowed us to capture consecutive steps during mitoribosomal large subunit (mt-LSU) biogenesis that involve normally short-lived assembly intermediates. Our structures provide important insights into the last steps of 16S rRNA folding, methylation and peptidyl transferase centre (PTC) completion, which require the coordinated action of nine assembly factors. We show that mammalian-specific MTERF4 contributes to the folding of 16S rRNA, allowing 16S rRNA methylation by MRM2, while GTPBP5 and NSUN4 promote fine-tuning rRNA rearrangments leading to PTC formation. Moreover, our data reveal an unexpected role for the elongation factor mtEF-Tu in mt-LSU assembly, in which mt-EF-Tu interacts with GTPBP5 in a manner similar to its interaction with tRNA during translational elongation. Together, our approaches provide detailed understanding of the last stages of mt-LSU biogenesis that are unique to mammalian mitochondria.

Main

Mammalian mitoribosomes assemble in a multi-step process that includes the maturation of two ribosomal RNAs (rRNAs; 12S and 16S), a structural tRNA, and incorporation of 82 mitoribosomal proteins (MRPs) [7]. Multiple assembly factors, many specific to mammalian mitochondria, assist in the mitoribosome assembly process. A growing number of studies in recent years have shown that a family of GTP-binding proteins (GTPBPs) is crucial for mammalian mitoribosome assembly [8–13]. Among these GTPBPs, GTPBP5 participates in the late steps of large subunit (mt-LSU) maturation, and its deletion leads to severe translational defects [8,11].

To understand the molecular basis for the late stages of human mitochondrial mt-LSU assembly, we used single-particle electron cryomicroscopy (cryo-EM) to determine the structure of an mt-LSU intermediate isolated from GTPBP5-deficient cells (GTPBP5^{KO}). In addition, we determined the cryo-EM structure of a GTPBP5-bound mt-LSU intermediate immunoprecipitated from cells expressing a tagged variant of GTPBP5 (GTPBP5^{IP}).

Composition of the GTPBP5^{KO} and GTPBP5^{IP} mt-LSU assembly intermediates

Both the GTPBP5^{KO} and GTPBP5^{IP} mt-LSU assembly-intermediates reveal several trapped assembly factors: the MTERF4-NSUN4 complex, MRM2, MTG1 and the MALSU1:L0R8F8:mt-ACP module (Fig. 1a,b, Extended Data Fig. 1 and 2). Furthermore, the GTPBP5^{IP} mt-LSU structure features GTPBP5 and the mitochondrial elongation factor mtEF-Tu (Fig. 1b, Extended Data Fig. 2). Comparing the GTPBP5^{KO} and the GTPBP5^{IP} mt-LSU intermediates with the mature mt-LSU [14] reveals two crucial differences in the 16S rRNA conformation (Fig. 1c,d). First, in both GTPBP5^{KO} and GTPBP5^{IP} intermediates, MTERF4 in the MTERF4-NSUN4 complex, binds an immaturely folded region of the 16S domain IV. This region (C2548-G2631) – corresponding to helices H68, H69, and H71 of the mature mt-LSU – is folded into a novel intermediate rRNA helical structure, hereafter denoted helix-X (Fig. 1). The helix-X occupies a different position on the mt-LSU than H68-71 in the mature mt-LSU, where helices H68-71 and H89-90 jointly form the peptidyl-transferase centre (PTC) (Fig. 1d). MTERF4s binding of helix-X partly orders the disordered rRNA in the mt-LSU assemblies' subunit interface side (Extended Data Fig. 1) and thereby enables MRM2 to bind (Fig. 1d). Second, in the GTPBP5^{KO} – but not in the GTPBP5^{IP} – the junction between H89 and H90 of domain V is significantly different compared to the mature mitoribosome (Fig. 1c, d). Specifically, at the base of H89, one helical turn remains unfolded and instead forms a flexible loop in the GTPBP5^{KO} (Fig. 1d).

MTERF4-NSUN4 complex steers the final steps of 16S rRNA folding and allows for MRM2 binding

The MTERF4-NSUN4 complex, previously shown to be essential for monosome assembly [16,17], binds at the intersubunit interface in our GTPBP5[KO] and GTPBP5[IP] structures (Fig. 1a, b). The C-terminal part of MTERF4 binds to NSUN4 close to the NSUN4 N-terminus in a mixed hydrophobic-polar binding interface similar to earlier crystal structures of the isolated complex [18,19] (Fig. 2a). NSUN4 was previously shown to m^{5}C-methylate the C1488 carbon 5 in 12S mt-rRNA [17]. In our structures, the active site of NSUN4 is turned towards the mt-LSU core (Extended Data Fig. 3a), impeding methylation of the 12S mt-rRNA. Although the methyl-donor S-adenosyl-methionine (SAM) is observed in the NSUN4 active site, no RNA substrate is present. Furthermore, in the GTPBP5[KO] and GTPBP5[IP] structures, the MTERF4-NSUN4 complex is bound and bent from two sides by uL2m. Specifically, a uL2m C-terminal extension penetrates in between NSUN4 and MTERF4 to further stabilize the MTERF4-NSUN4 binding interface and decreases the curvature of the MTERF4 solenoid relative to the crystal structures (Fig. 2a). This reforming of the MTERF4 solenoid is necessary to bind the helix-X rRNA region in the strongly positively charged concave side of MTERF4 (Extended Data Fig. 3b). Here, MTERF4 forms an extensive network of contacts with helix-X that stabilizes the association and promotes helix-X folding (Fig. 2b). The mature H71 base-pairing is already formed within helix-X. Thus, by binding to helix-X, MTERF4 intiates the folding of this 16S mt-rRNA region. Furthermore, it also exposes the A-loop, which is obstructed by H68, H69, and H71 in the mature mt-LSU (Fig. 1d), thereby allowing MRM2 binding.

Similarly to a previously determined mt-LSU assembly intermediate [20] there is a MALSU1-module positioned adjacent to uL14m in both the GTPBP5[KO] and GTPBP5[IP] (Fig.1a,b). Furthermore, MTG1 (GTPBP7), which assists in late-stage mt-LSU maturation [21], is bound in the vicinity of helix-X (Fig. 1a,b). MTG1 contacts the C-terminus of MALSU1 (Extended Data Fig. 4a) and the region encompassing A2554-U2602 of helix-X. This region could not modelled due to the lower local resolution, but the contact is visible in the electron density map (Extended Data Fig. 4b). Interestingly, the position of human MTG1 in our structures differs significantly from its bacterial and trypanosomal counterparts ([3,22], Extended Data Fig. 4c). Specifically, while in other systems MTG1 homologs contact the rRNA, reaching out towards the PTC (Extended Data Fig. 4c), in the trapped intermediates described here MTG1 is unlikely to induce pronounced conformational changes of the PTC or participate in the recruitment/dissociation of assembly factors.

137   MRM2 2′-O-methylates U3039 in the 16S A-loop during mt-LSU assembly [23,24] and

138   in our GTPBP5^{KO} and GTPBP5^{IP} structures, MRM2 binds in the mt-LSU intersubunit

139   interface (Fig. 1a,b). It features two N-terminal α-helices followed by a canonical S-adenosyl-

140   L-methionine-dependent methyltransferase domain (SAM MTase) (Fig. 2c). In GTPBP5^{KO},

141   but not in GTPBP5^{IP}, the two N-terminal α-helices extend from MRM2 and insert into the

142   rRNA core to thereby displace and retrieve the A-loop (16S mt-rRNA domain V) through a

143   complex interaction network (Fig. 2d,e). This places the 2′-hydroxyl of U3039 close to the

144   ideal methyl-acceptor position in the MRM2 active site (Fig. 2d). However, there is no

145   density for either SAM or S-adenosyl homocysteine (SAH) in the MRM2 active site and there

146   is no apparent density for a 2′-O-methyl on U3039 (Extended Data Fig. 5). Interestingly,

147   G3040 that is 2′-O-methylated by MRM3 [23,24], is methylated in our structures (Extended Data

148   Fig. 5). Hence, 2′-O-methylation by MRM3 takes place prior to MRM2 methylation in human

149   mitoribosome biogenesis.

150

GTPBP5 promotes remodelling of the PTC

152   GTPBP5 consists of a glycine-rich N-terminal domain (Obg-domain) and a C-terminal

153   GTPase domain (G-domain) (Fig. 3a). In our GTPBP5^{IP} structure, the G-domain has GTP in

154   its active site and is wedged between the L7/L12 stalk and the MALSU1 module (Fig. 1b and

155   Extended Data Fig. 6a). The Obg-domain protrudes into the PTC (Fig. 3b), thereby displacing

156   the A-loop from the MRM2 active site and expelling the MRM2 N-terminal α-helices from

157   the rRNA core (Fig. 3c), while the A-loop folds into the fully mature position (Fig. 3b3).

158   The protruding Obg-domain is positioned between H89 and H93 and occupies the space that

159   accommodates the acceptor arm of the A-site tRNA during translation (Extended Data Fig.

160   6b). Hereby, GTPBP5 adopts a tRNA mimicry strategy, similar to ObgE of *E. coli* [25]. The

161   Obg-domain contains six glycine-rich sequence motifs that form antiparallel polyproline-II

162   helices (helices a–f) (Fig. 3b). Helices c and d bind the A-loop, while the loop between

163   helices e and f inserts into the major groove of H93. The loop between a and b inserts at the

164   triple-junction formed between H89-H90-H93 (Fig. 3b).

165   Comparison of the GTPBP5^{KO} and the GTPBP5^{IP} structures with the mature mt-LSU reveals

166   extensive maturation of the PTC upon GTPBP5 binding. The partly unfolded H89 in the

167   GTPBP5^{KO} is folded in the GTPBP5^{IP} (Fig. 3 b1). This folding is coordinated by the joint

168   action of GTPBP5 and NSUN4: in the presence of GTPBP5, the extended N-terminal region

169   of NSUN4 inserts into the rRNA core and temporarily displaces the P-loop (Fig. 3 b2),

170   thereby breaking the P-loop interaction with H89 (Fig. 3d). As a consequence, H89 is given

171   the space necessary to fold into a structure similar to its mature form (Fig. 3 b1, lower).

172   The GTPBP5[IP] structure shows a rotation of the L7/L12 stalk in comparison to the GTPBP5[KO]

173   structure (Extended Data Fig. 6c). Here, the rRNA in the L54/L11 region of the stalk forms π-

174   stacking interactions with two residues of the GTP-ase switch I element of GTPBP5

175   (Extended Data Fig. 6a,c). Thereby, the L7/L12 stalk stabilizes the "state 2" conformation of

176   the switch I. In this way, the rotated L7/L12 stalk stabilizes the GTP-state of GTPBP5[26] and

177   consequently a GTP is bound in our structure (Extended Data Fig. 6a,c). The requirement for

178   GTPBP5 to be in a GTP-bound state is supported by the inability of a GTPBP5 Walker A

179   mutant (GTPBP5-S238A) to bind mt-LSU intermediates [8]. A back-rotation of the L7/12 stalk,

180   presumably by binding of another maturation factor to the mt-LSU assembly intermediate,

181   would lead to a release of the switch I and the activation of GTP hydrolysis, followed by

182   release of GTPBP5 from the mt-LSU assembly intermediate. Taken together, GTPBP5 plays

183   a direct and active role in rRNA remodeling and, together with the NSUN4 N-terminus,

184   orchestrates the maturation of mitoribosomal PTC.

185

186   **Translation elongation factor mtEF-Tu is involved in mitoribosome assembly**

187   mtEF-Tu consists of a GTPase domain (G-domain; domain I) and two structurally

188   similar β-stranded domains (domains II and III) (Fig. 4a). It was recently shown that during

189   translation, mtEF-Tu·GTP delivers aminoacylated-tRNA to the mitoribosome in a manner

190   similar to its bacterial EF-Tu counterparts (Extended Data Fig. 7a,[27]). In contrast, the binding

191   of an EF-Tu·GTP·aa-tRNA complex is sterically hindered by the MALSU1 module bound in

192   our mt-LSU intermediates (Extended Data Fig. 7a). Unexpectedly, mtEF-Tu binds to the

193   mitoribosome in a unique manner in our GTPBP5[IP] structure (Fig. 4b). Here, domains II and

194   III establish extensive interactions with GTPBP5, the sarcin-ricin loop (SRL) and the

195   MALSU1 stalk (Fig. 4b,c). In addition, the G-domain switch I element, in its "state 1"/GDP

196   conformation (Extended Data Fig. 7b), extends and binds MALSU1. Thereby, mtEF-Tu,

197   together with the SRL and MALSU1, forms a platform for GTPBP5 binding (Fig. 4b). These

198   structural conclusions are supported by earlier mass-spectrometry data on isolated GTPBP5[IP]

199   assembly intermediates and protein-proximity interactome analysis [8,28].

200   The G-domain of mtEF-Tu does not contact the SRL as in mtEF-Tu's canonical role in

201   translation but instead binds to the C-terminal region of a bL12m that also contacts uL10m at

202   the stalk base (Fig. 4b). In bacteria, homologs to bL12m and uL10m, recruit and activate

6

203   translational GTPases such as EF-Tu via the bL12m C-terminal domain[29,30] and stimulate
204   GTP hydrolysis 1000-fold[31]. Taken together, this suggests that mtEF-Tu hydrolysis –
205   stimulated by bL12m and uL10m – is used to accommodate GTPBP5 on the maturating mt-
206   LSU in analogy to the canonical EF-Tu role in translation, in which aminoacylated-tRNA is
207   accommodated on the translating ribosome (Extended Data Fig. 7a).

208
209   **Concluding remarks**

210   Our analyses shed new light into mammalian mitoribosome maturation and explain
211   the essential roles of several assembly factors that together promote fine RNA rearrangments
212   and lead to the mt-LSU completion. Thanks to our approaches that combine biochemical tools
213   with structural determination, we were able to uncovered several features unique to
214   mammalian mitochondria. Based on these data, we propose a model of the late-stage mt-
215   LSU assembly that requires the interplay of nine auxiliary factors (Fig. 4d).

216   Lastly, as defects in mitoribosome biogenesis – resulting from, for example, mutations
217   in MRM2 and GTPBP5 – are increasingly implicated in mitochondrial disease [32,33], the
218   current work does not only describes fundamental cellular processes but may also further new
219   diagnostic and therapeutic approaches to mitochondrial diseases.

220
221   **Methods**

222
223   **Generation of GTPBP5 knock-out cell line**
224   The knock-out cell line (GTPBP5[KO]) was generated in the Flp-In T-Rex human embryonic
225   kidney 293 (HEK293T) cell line (Invitrogen) using CRISPR/Cas9 technology targeted on
226   exon 1 of *MTG2* gene, which encodes for GTPBP5, as described [8]. In short, two pairs of
227   gRNAs were designed and cloned into the pSpCas9(BB)-2A-Puro (pX459) V2.0 vector to
228   generate out-of-frame deletions. Transfection of HEK293T cell line with the pX459 variants
229   was performed using Lipofectamine 3000 following manufacturer's instructions. Selection of
230   transfected cells was done using puromycin treatment at a final concentration of 1.5 mg/ml
231   for 48 hours. Subsequently, cells were single-cell diluted and transferred into a 96-well plate.
232   Selected clones were screened via Sanger sequencing and Western blotting.

233
234   **Purification of the mt-LSU from GTPBP5[KO] cell line via sucrose gradient centrifugation**
235   Isolation of mitochondria was performed from GTPBP5[KO] cell line as described in Rorbach *et*
236   *al.* [24], with some modifications. Crude mitochondria were further purified via differential

237   centrifugation by being loaded onto a sucrose gradient (1 M and 1.5 M sucrose, 20 mM

238   Tris-HCl pH 7.5, 1 mM EDTA) and centrifuged at 25000 rpm for 1 hour at 4°C (Beckman

239   Coulter SW41-Ti rotor). Mitochondria forming a band at the interphase between the 1 M and

240   1.5 M sucrose were collected and resuspended in 10 mM Tris-HCl pH = 7.5 in 1:1 ratio. After

241   centrifugation, the final mitochondrial pellet was resuspended in mitochondrial freezing

242   buffer (200 mM trehalose, 10 mM Tris-HCl pH 7.5, 10 mM KCl, 0.1% BSA, 1 mM

243   EDTA), snap frozen in liquid nitrogen and stored at -80°C.

244   The mt-LSU was purified from the GTPBP5[KO] cell line via a sucrose gradient centrifugation

245   experiment. Mitochondria were lysed at 4°C for 20 minutes (25 mM HEPES-KOH pH = 7.5,

246   20 mM $Mg(OAc)_2$, 100 mM KCl, 2% (v/v) Triton X-100, 2 mM dithiothreitol (DTT), 1x

247   cOmplete EDTA-free protease inhibitor cocktail (Roche), 40 U/µl RNase inhibitor

248   (Invitrogen)) and later centrifuged at 13000 rpm for 5 minutes at 4°C. For mitoribosome

249   purification, the mitolysate was subjected to sucrose cushion ultracentrifugation method (0.6

250   M sucrose, 25 mM HEPES-KOH pH = 7.5, 10 mM $Mg(OAc)_2$, 50 mM KCl, 0.5% (v/v)

251   Triton X-100, 2 mM DTT) by being centrifuged at 73000 rpm for 45 minutes at 4°C

252   (Beckman Coulter TL120.2 rotor). The mitoribosomal pellet was subsequently resuspended in

253   ribosome resuspension buffer (25 mM HEPES-KOH pH = 7.5, 10 mM $Mg(OAc)_2$, 50 mM

254   KCl, 0.05% DDM, 2 mM DTT) and centrifuged at 13000 rpm for 10 minutes at 4°C. The

255   obtained supernatant was then loaded onto a linear sucrose gradient (15-30% (w/v)) in 1x

256   gradient buffer (25 mM HEPES-KOH pH = 7.5, 10 mM $Mg(OAc)_2$, 50 mM KCl, 0.05%

257   DDM, 2 mM DTT) and centrifuged for 2 hours and 15 minutes at 39000 rpm at 4°C

258   (Beckman Coulter TLS55 rotor). Fractions corresponding to the large mitochondrial subunit

259   were collected and subjected to buffer exchange (25 mM HEPES-KOH pH = 7.5, 10 mM

260    $Mg(OAc)_2$, 50 mM KCl) using Vivaspin 500 centrifugal concentrators.

261

262   **Generation of a mammalian cell line expressing GTPBP5**

263   A stable mammalian cell line overexpressing C-terminal FLAG-tagged GTPBP5

264   (GTPBP5::FLAG) in a doxycycline-inducible dose-dependent manner was generated as

265   described in Cipullo et al. [8]. The GTPBP5 cDNA (hORFeome Database; Internal ID: 12579)

266   was cloned into pcDNA5/FRT/TO. Flp-In T-Rex human embryonic kidney 293 (HEK293T,

267   Invitrogen) cells were cultured in DMEM (Dulbecco's modified eagle medium) containing

268   10% (v/v) tetracycline-free fetal bovine serum (FBS), 2 mM Glutamax (Gibco), 1x

269   Penicillin/Streptomycin (Gibco), 50 µmg/ml uridine, 10 µg/ml Zeocin (Invitrogen) and 100

270   µg/ml blasticidin (Gibco) at 37 °C under 5% CO_2 atmosphere. Cells were seeded in a 6-well

271 plate, grown in medium without antibiotics and co-transfected with pcDNA5/FRT/TO-
272 GTPBP5::FLAG and pOG44 using Lipofectamine 3000 according to manufacturer's
273 recommendations. After 48 hours, selection of cells was promoted by addition of hygromycin
274 (100 µg/ml, Invitrogen) and blasticidin (100 µg/ml) to culture media. After two to three
275 weeks post-transfection, single colonies were picked and GTPBP5 overexpression was tested
276 via Western Blot analysis 48 hours after induction with 50 ng/ml doxycycline.

277

Immunoprecipitation experiment

279 Isolation and purification of mitochondria from GTPBP5::FLAG overexpressing cell line was
280 performed as described in the above paragraph "Purification of the mt-LSU from GTPBP5^{KO}
281 cell line via sucrose gradient centrifugation". The mt-LSU bound with GTPBP5 was isolated
282 via FLAG-immunoprecipitation analysis (IP). Pelleted mitochondria were lysed at 4°C for 20
283 minutes (25 mM HEPES-KOH pH = 7.5, 20 mM Mg(OAc)$_2$, 100 mM KCl, 2% (v/v) Triton
284 X-100, 0.2 mM DTT, 1x cOmplete EDTA-free protease inhibitor cocktail (Roche), 40 U/□l
285 RNase inhibitor (Invitrogen)) and centrifuged at 5000g for 5 minutes at 4°C. The supernatant
286 was then added to ANTI-FLAG M2-Agarose Affinity Gel (Sigma-Aldrich) previously
287 equilibrated (25 mM HEPES-KOH pH = 7.5, 5 mM Mg(OAc)$_2$, 100 mM KCl, 0.05% DDM)
288 and incubated for 3 hours at 4°C. After incubation, the sample was centrifuged at 5000g for 1
289 minute at 4°C, the supernatant was removed and the gel was washed three times with wash
290 buffer. Elution (25 mM HEPES-KOH pH = 7.5, 5 mM Mg(OAc)$_2$, 100 mM KCl, 0.05%
291 DDM, 2 mM DTT) was performed using 3x FLAG Peptide (Sigma-Aldrich) for about 40
292 minutes at 4°C.

293

Cryo-EM data acquisition and image processing

295 Prior to cryo-EM grid preparation, grids were glow-discharged with 20 mA for 30 seconds
296 using a PELCO easiGlow glow-discharge unit. Quantifoil Cu 300 mesh (R 2/2 geometry;
297 Quantifoil Micro Tools GMBH) covered with a thin layer of 3 nm carbon were used for the
298 for the GTPBP5^{KO} sample. Carbon lacey films (400 mesh Cu grid; Agar Scientific) mounted
299 with ultrathin carbon support film were used for the GTPBP5^{IP} sample. Three □l aliquots of
300 sample were applied to the grids, which were then vitrified in a Vitrobot Mk IV (Thermo
301 Fisher Scientific) at 4°C and 100% humidity (blot 10 s, blot force 3, 595 filter paper (Ted
302 Pella Inc.)). Cryo-EM data collection (Extended Data Table 1) was performed with EPU
303 (Thermo Fisher Scientific) using a Krios G3i transmission-electron microscope (Thermo
304 Fisher Scientific) operated at 300 kV in the Karolinska Institutet's 3D-EM facility. Images

305 were acquired in nanoprobe EFTEM SA mode with a slit width of 10 eV using a K3

306 Bioquantum during 1 second during which 60 movie frames were collected with a flux of

307 0.82 e$^-$/Å^2 per frame. Motion correction, CTF-estimation, Fourier binning (to 1.02 Å/px),

308 picking and extraction in 600 pixel boxes (size threshold 300 Å, distance threshold 20 Å,

309 using the pretrained BoxNet2Mask_20180918 model) were performed on the fly using Warp

310 [34]. Only particles from micrographs with an estimated resolution of 3.6 Å and underfocus

311 between 0.2 and 3 □m were retained for further processing.

312 For the GTPBP5^{KO} dataset, 704720 particles were picked from 37307 micrographs (Extended

313 Data Fig. 1). The particles were imported into CryoSPARC 2.15 [35] for further processing.

314 After 2D classification, 130289 particles were selected for an ab-initio reconstruction. This

315 reconstruction, in addition to two "bad" reconstructions created from bad 2D class-averages,

316 were used for heterogeneous refinement of the complete particle set resulting in one of the

317 three classes yielding a large-subunit reconstruction with high resolution features (196318

318 particles). After homogeneous refinement of these particles, the PDB model of a

319 mitochondrial LSU assembly intermediate (PDB: 5OOL [20]) was fitted in the density. The

320 reconstruction contained the MALSU1 module and also featured weak unexplained densities

321 for several additional components in the intersubunit interface. A 3D variability analysis was

322 performed with a mask on the intersubunit interface and a low pass resolution of 10 Å, and

323 subsequently used for clustering into six particle classes representing different assembly

324 intermediates. Two of the classes (43057 and 41619 particles) lacked the density for the A-

325 and P-loops, H89, helices 68-71 and the L7/12 stalk. The A- and P-loops become visible in

326 the third class (28001 particles). The fourth class revealed a number of biogenesis factors:

327 MRM2, MTERF4-NSUN4, MTG1 and the structured H67-H71 rRNA region (helix-X)

328 (48646 particles) as well as H89. All the biogenesis factors are absent in the fifth class, in

329 which helices 68 and 71 move to the mature position (26678 particles). H69 is nevertheless

330 not visible. The last class contains the small subunit (8317 particles). Non-uniform refinement

331 of the fourth particle set yielded a reconstruction at 2.64. Å, which was used for model

332 building and refinement. As the density for MTG1 was weaker than for the other factors, 3D

333 variability analysis was performed with a mask on the MTG1 region and a 10 Å low-pass

334 filter to select particles containing MTG1 (19254 particles, which was subsequently subjected

335 to homogeneous refinement yielding a reconstruction at 2.90 Å).

336 For the GTPBP5^{IP} dataset, 283598 particles were picked from 112076 micrographs using

337 WARP and imported into CryoSPARC 2.15 (Extended Data Fig. 2) [35]. The complete particle

338 set was used in heterogeneous refinement against the same three references derived from the

10

339   GTPBP5[KO] dataset. One of the classes (78306 particles) yielded a high-resolution

340   reconstruction of the mt-LSU assembly intermediate. After homogeneous refinement,

341   additional density for GTPBP5 was visible in the intersubunit interface. 3D variability

342   analysis was performed with a mask on the GTPBP5 region and a low pass resolution of 10

343   Å. Subsequent clustering into two particle clusters revealed a particle subset containing

344   GTPBP5 (71834 particles), which was used for model building and refinement. This

345   reconstruction also features densities for MRM2 and MTERF4-NSUN4. In addition, a weak

346   density was present for mtEF-TU, the bL12m C-terminal domain and MTG1. The refined

347   particles were subject to 2D classification and the bad classes were removed. The remaining

348   particles were polished and refined in Relion 3.1 and re-imported into CryoSPARC for further

349   processing. 3D variability analysis was performed on these particles with a mask covering

350   mtEF-TU, bL12m and MTG1 and a 10 Å low pass filter. Subsequent clustering (4 clusters)

351   revealed 2 clusters containing mtEF-TU/bL12m (17886 particles in total), one cluster

352   containing MTG1 (8233 particles) and one cluster containing all three proteins (13376

353   particles). The reconstructions derived from the MTG1- and the mtEF-Tu-containing particles

354   reached a resolution of 3.19 and 3.21 Å respectively.

355

356   **Model building and refinement**

357   Model building of the GTPBP5[KO] and GTPBP5[IP] mt-LSU assembly intermediate structures

358   was performed using *Coot* [36]. The structure of a previous mt-LSU assembly intermediate

359   (PDB 5OOL, [20]) was used as a starting model. MRM2 and MTERF4-NSUN4 were identified

360   by modelling secondary structure elements in *Coot*, and using the initial models for a

361   structural search using the DALI server [37]. MTG1, as well as mtEF-Tu and the bL12m C-

362   terminal domain in the GTPBP5-bound mt-LSU dataset, were identified using a density-based

363   fold-recognition pipeline [20]. Using SWISS-MODEL [38], we generated homology models for

364   the human GTPBP5 (template: PDB 4CSU chain 9 [25]), MTG1 (template: PDB 3CNL chain A

365   [39]), bL12m (template: PDB 1DD3 chain A [40]) and mtEF-TU (template: PDB 1D2E chain A

366   [41]). All the models, as well as the crystal structure of the human MTERF4-NSUN4 (template:

367   PDB 4FP9 chains A and B [18]), were fitted into the density map using *Coot* JiggleFit. The

368   MTG1 GTPase domain and the L17/12 stalk were excluded from atomic refinement and were

369   only subject to rigid body refinement. Metal ions and modifications were placed based on

370   map densities. Stereochemical refinement was performed using PHENIX [42]. Refinement

371   statistics are reported in Extended Data Table 2, while modeled proteins and rRNA are shown

372 in Extended Data Table 3. Validation of the final models was done via MolProbity [43]. Figures

373 were generated using ChimeraX [44].

374

375 **References**

376 1. Hällberg, B. M. & Larsson, N.-G. Making Proteins in the Powerhouse. *Cell Metab.* **20**,

377 226–240 (2014).

378 2. Greber, B. J. *et al.* The complete structure of the 55S mammalian mitochondrial

379 ribosome. *Science (80-.).* **348**, 303–308 (2015).

380 3. Jaskolowski, M. *et al.* Structural Insights into the Mechanism of Mitoribosomal Large

381 Subunit Biogenesis. *Mol. Cell* **79**, 629-644.e4 (2020).

382 4. Saurer, M. *et al.* Mitoribosomal small subunit biogenesis in trypanosomes involves an

383 extensive assembly machinery. *Science (80-.).* **365**, 1144–1149 (2019).

384 5. Perez Boerema, A. *et al.* Structure of the chloroplast ribosome with chl-RRF and

385 hibernation-promoting factor. *Nat. Plants* **4**, 212–217 (2018).

386 6. Amunts, A., Brown, A., Toots, J., Scheres, S. H. W. & Ramakrishnan, V. The structure

387 of the human mitochondrial ribosome. *Science (80-.).* **348**, 95–98 (2015).

388 7. Bogenhagen, D. F., Ostermeyer-Fay, A. G., Haley, J. D. & Garcia-Diaz, M. Kinetics

389 and Mechanism of Mammalian Mitochondrial Ribosome Assembly. *Cell Rep.* **22**,

390 1935–1944 (2018).

391 8. Cipullo, M. *et al.* Human GTPBP5 is involved in the late stage of mitoribosome large

392 subunit assembly. *Nucleic Acids Res.* (2020) doi:10.1093/nar/gkaa1131.

393 9. Lavdovskaia, E. *et al.* The human Obg protein GTPBP10 is involved in mitoribosomal

394 biogenesis. *Nucleic Acids Res.* **46**, 8471–8482 (2018).

395 10. Maiti, P., Kim, H.-J., Tu, Y.-T. & Barrientos, A. Human GTPBP10 is required for

396 mitoribosome maturation. *Nucleic Acids Res.* (2018) doi:10.1093/nar/gky938.

397 11. Maiti, P., Antonicka, H., Gingras, A.-C., Shoubridge, E. A. & Barrientos, A. Human

398 GTPBP5 (MTG2) fuels mitoribosome large subunit maturation by facilitating 16S

399 rRNA methylation. *Nucleic Acids Res.* **48**, 7924–7943 (2020).

400 12. Kim, H.-J. & Barrientos, A. MTG1 couples mitoribosome large subunit assembly with

401 intersubunit bridge formation. *Nucleic Acids Res.* **46**, 8435–8453 (2018).

402 13. Lavdovskaia, E. *et al.* Dual function of GTPBP6 in biogenesis and recycling of human

403 mitochondrial ribosomes. *Nucleic Acids Res.* **48**, 12929–12942 (2020).

404 14. Brown, A. *et al.* Structure of the large ribosomal subunit from human mitochondria.

405 *Science (80-.).* **346**, 718–722 (2014).

12

406   15.   Aibara, S., Singh, V., Modelska, A. & Amunts, A. Structural basis of mitochondrial
407   translation. *Elife* **9**, (2020).

408   16.   Cámara, Y. *et al.* MTERF4 Regulates Translation by Targeting the Methyltransferase
409   NSUN4 to the Mammalian Mitochondrial Ribosome. *Cell Metab.* **13**, 527–539 (2011).

410   17.   Metodiev, M. D. *et al.* NSUN4 Is a Dual Function Mitochondrial Protein Required for
411   Both Methylation of 12S rRNA and Coordination of Mitoribosomal Assembly. *PLoS*
412   *Genet.* **10**, e1004110 (2014).

413   18.   Spåhr, H., Habermann, B., Gustafsson, C. M., Larsson, N.-G. & Hallberg, B. M.
414   Structure of the human MTERF4–NSUN4 protein complex that regulates
415   mitochondrial ribosome biogenesis. *Proc. Natl. Acad. Sci.* **109**, 15253–15258 (2012).

416   19.   Yakubovskaya, E. *et al.* Structure of the Essential MTERF4:NSUN4 Protein Complex
417   Reveals How an MTERF Protein Collaborates to Facilitate rRNA Modification.
418   *Structure* **20**, 1940–1947 (2012).

419   20.   Brown, A. *et al.* Structures of the human mitochondrial ribosome in native states of
420   assembly. *Nat. Struct. Mol. Biol.* **24**, 866–869 (2017).

421   21.   Kim, H. J. & Barrientos, A. MTG1 couples mitoribosome large subunit assembly with
422   intersubunit bridge formation. *Nucleic Acids Res.* **46**, 8435–8453 (2018).

423   22.   Seffouh, A. *et al.* Structural consequences of the interaction of RbgA with a 50S
424   ribosomal subunit assembly intermediate. *Nucleic Acids Res.* **47**, 10414–10425 (2019).

425   23.   Lee, K. W. & Bogenhagen, D. F. Assignment of 2′-O-methyltransferases to
426   modification sites on the mammalian mitochondrial large subunit 16 S ribosomal RNA
427   (rRNA). *J. Biol. Chem.* **289**, 24936–24942 (2014).

428   24.   Rorbach, J. *et al.* MRM2 and MRM3 are involved in biogenesis of the large subunit of
429   the mitochondrial ribosome. *Mol. Biol. Cell* **25**, 2542–2555 (2014).

430   25.   Feng, B. *et al.* Structural and Functional Insights into the Mode of Action of a
431   Universally Conserved Obg GTPase. *PLoS Biol.* **12**, e1001866 (2014).

432   26.   Matsumoto, S. *et al.* Molecular Mechanism for Conformational Dynamics of Ras·GTP
433   Elucidated from In-Situ Structural Transition in Crystal. *Sci. Rep.* **6**, 25931 (2016).

434   27.   Desai, N. *et al.* Elongational stalling activates mitoribosome-associated quality control.
435   *Science (80-.).* **370**, 1105–1110 (2020).

436   28.   Antonicka, H. *et al.* A High-Density Human Mitochondrial Proximity Interaction
437   Network. *Cell Metab.* **32**, 479-497.e9 (2020).

438   29.   Traut, R. R. *et al.* Location and domain structure of Escherichia coli ribosomal protein
439   L7/L12: site specific cysteine cross-linking and attachment of fluorescent probes.

440   *Biochem. Cell Biol.* **73**, 949–958 (1995).

441   30.   Mustafi, M. & Weisshaar, J. C. Simultaneous Binding of Multiple EF-Tu Copies to

442   Translating Ribosomes in Live Escherichia coli. *MBio* **9**, (2018).

443   31.   Diaconu, M. *et al.* Structural Basis for the Function of the Ribosomal L7/12 Stalk in

444   Factor Binding and GTPase Activation. *Cell* **121**, 991–1004 (2005).

445   32.   Garone, C. *et al.* Defective mitochondrial rRNA methyltransferase MRM2 causes

446   MELAS-like clinical syndrome. *Hum. Mol. Genet.* **26**, 4257–4266 (2017).

447   33.   Solomon, B. D. *et al.* De novo deletion of chromosome 20q13.33 in a patient with

448   tracheo-esophageal fistula, cardiac defects and genitourinary anomalies implicates

449   GTPBP5 as a candidate gene. *Birth Defects Res. Part A Clin. Mol. Teratol.* **91**, 862–

450   865 (2011).

451   34.   Tegunov, D. & Cramer, P. Real-time cryo-electron microscopy data preprocessing with

452   Warp. *Nat. Methods* **16**, 1146–1152 (2019).

453   35.   Punjani, A., Rubinstein, J. L., Fleet, D. J. & Brubaker, M. A. cryoSPARC: algorithms

454   for rapid unsupervised cryo-EM structure determination. *Nat. Methods* **14**, 290–296

455   (2017).

456   36.   Emsley, P., Lohkamp, B., Scott, W. G. & Cowtan, K. Features and development of

457   Coot. *Acta Crystallogr. Sect. D Biol. Crystallogr.* **66**, 486–501 (2010).

458   37.   Holm, L. DALI and the persistence of protein shape. *Protein Sci.* **29**, 128–140 (2020).

459   38.   Arnold, K., Bordoli, L., Kopp, J. & Schwede, T. The SWISS-MODEL workspace: a

460   web-based environment for protein structure homology modelling. *Bioinformatics* **22**,

461   195–201 (2006).

462   39.   Kim, D. J., Jang, J. Y., Yoon, H.-J. & Suh, S. W. Crystal structure of YlqF, a circularly

463   permuted GTPase: Implications for its GTPase activation in 50 S ribosomal subunit

464   assembly. *Proteins Struct. Funct. Bioinforma.* **72**, 1363–1370 (2008).

465   40.   Wahl, M. C., Bourenkov, G. P., Bartunik, H. D. & Huber, R. Flexibility,

466   conformational diversity and two dimerization modes in complexes of ribosomal

467   protein L12. *EMBO J.* **19**, 174–186 (2000).

468   41.   Andersen, G. R., Thirup, S., Spremulli, L. L. & Nyborg, J. High resolution crystal

469   structure of bovine mitochondrial EF-tu in complex with GDP. *J. Mol. Biol.* **297**, 421–

470   436 (2000).

471   42.   Liebschner, D. *et al.* Macromolecular structure determination using X-rays, neutrons

472   and electrons: recent developments in Phenix. *Acta Crystallogr. Sect. D Struct. Biol.*

473   **75**, 861–877 (2019).

474   43.   Chen, V. B. *et al.* MolProbity□: all-atom structure validation for macromolecular

475   crystallography. *Acta Crystallogr. Sect. D Biol. Crystallogr.* **66**, 12–21 (2010).

476   44.   Goddard, T. D. *et al.* UCSF ChimeraX: Meeting modern challenges in visualization

477   and analysis. *Protein Sci.* **27**, 14–25 (2018).

478   45.   Rosenthal, P. B. & Henderson, R. Optimal Determination of Particle Orientation,

479   Absolute Hand, and Contrast Loss in Single-particle Electron Cryomicroscopy. *J. Mol.*

480   *Biol.* **333**, 721–745 (2003).

481   46.   Baker, N. A., Sept, D., Joseph, S., Holst, M. J. & McCammon, J. A. Electrostatics of

482   nanosystems: Application to microtubules and the ribosome. *Proc. Natl. Acad. Sci.* **98**,

483   10037–10041 (2001).

484   47.   Greber, B. J. *et al.* The complete structure of the 55S mammalian mitochondrial

485   ribosome. *Science (80-.).* **348**, 303–308 (2015).

486

487

488

489

490

498

499   **Author contributions:** M.C. with A.K and J.R. help performed cell biology, biochemistry

500   and sample preparations; G.V.G. and B.M.H. performed cryo-EM data collection; G.V.G. and

501   B.M.H. processed data and determined structures; G.V.G. built and refined models with help

502   from A.K. and B.M.H.; M.C. and G.V.G. wrote the manuscript with input from all authors;

503   J.R. and B.M.H. oversaw the project and edited the manuscript.

504

505   **Competing interests:** Authors declare no competing interests.
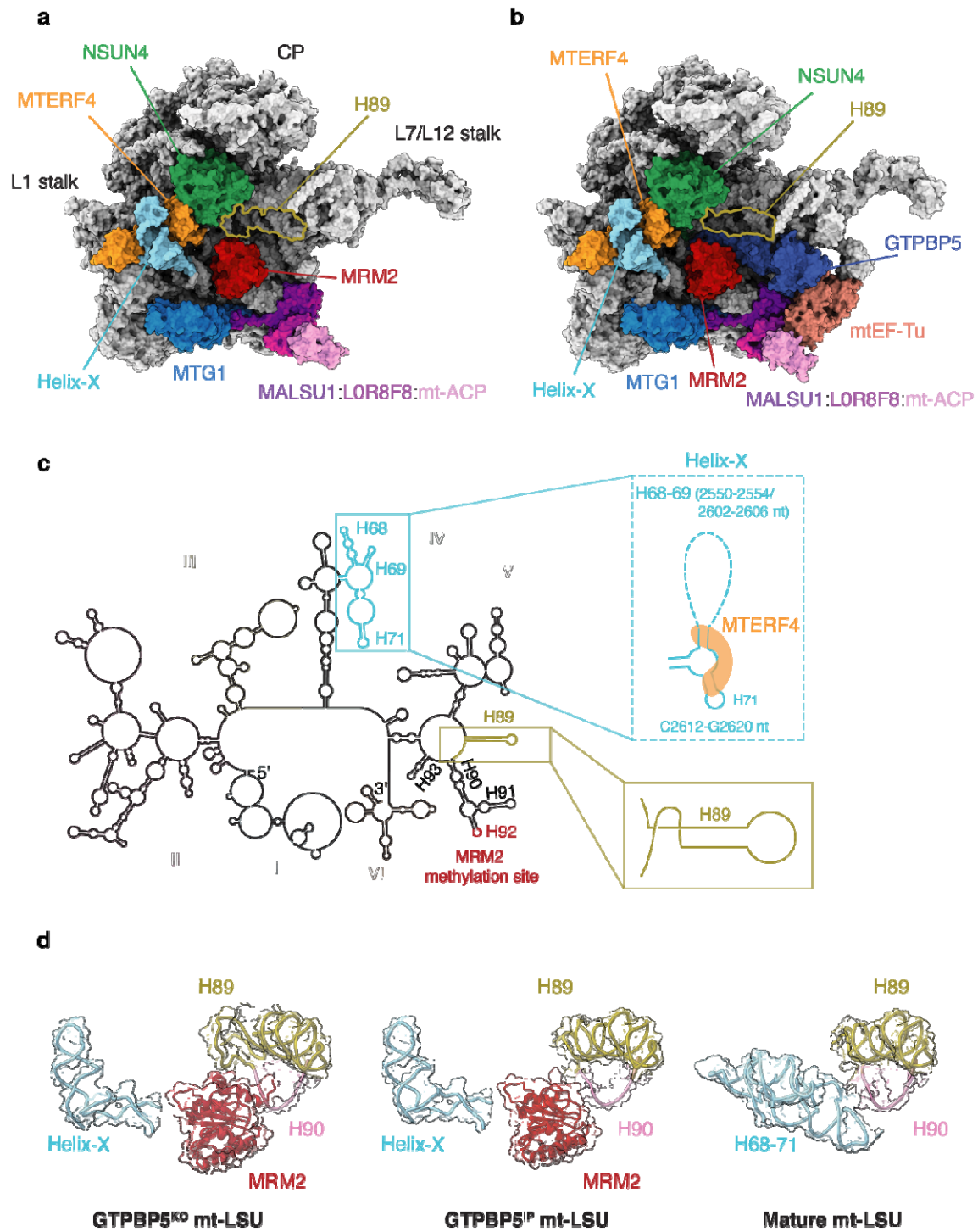
506

507

508

509

510

511

Fig. 1: Overview of the GTPBP5[KO] and the GTPBP5[IP] mt-LSU assembly intermediates and comparison with the mature mt-LSU. a, The GTPBP5[KO] is bound by MTERF4, NSUN4, MRM2, MTG1 and the MALSU1 module. Mitoribosomal proteins and 16S mt-rRNA are shown in grey. Helix-X bound to MTERF4 is highlighted as well as H89. **b,** The interface of the GTPBP5[IP] mt-LSU intermediate associated with MTERF4, NSUN4, MRM2, MTG1, MALSU1:L0R8F8:mt-ACP complex, GTPBP5 and mtEF-Tu. Helix-X bound to MTERF4 is shown in light blue. **c,** Secondary structure of the mature mt-LSU 16S mt-rRNA. Differences in the rRNA fold

519   of the GTPBP5^{KO} mt-LSU intermediate are shown in the zoomed-in views. Dashed lines indicate regions that are

520   not modelled. MRM2 methylation site (H92) is indicated in red. The six 16S mt-rRNA domains are shown in

521   different colours. **d**, Positioning of helix-X (H68-71) and helices H89 and H90 in GTPBP5^{KO} mt-LSU (left),

522   GTPBP5^{IP} mt-LSU (middle) and the mature mt-LSU (right) (PDB:6ZSG [15]). In the GTPBP5^{KO} and the

523   GTPBP5^{IP} mt-LSU structures MRM2 is present.

524

525

526

527

528

529

530

531

532

533

534

535

536
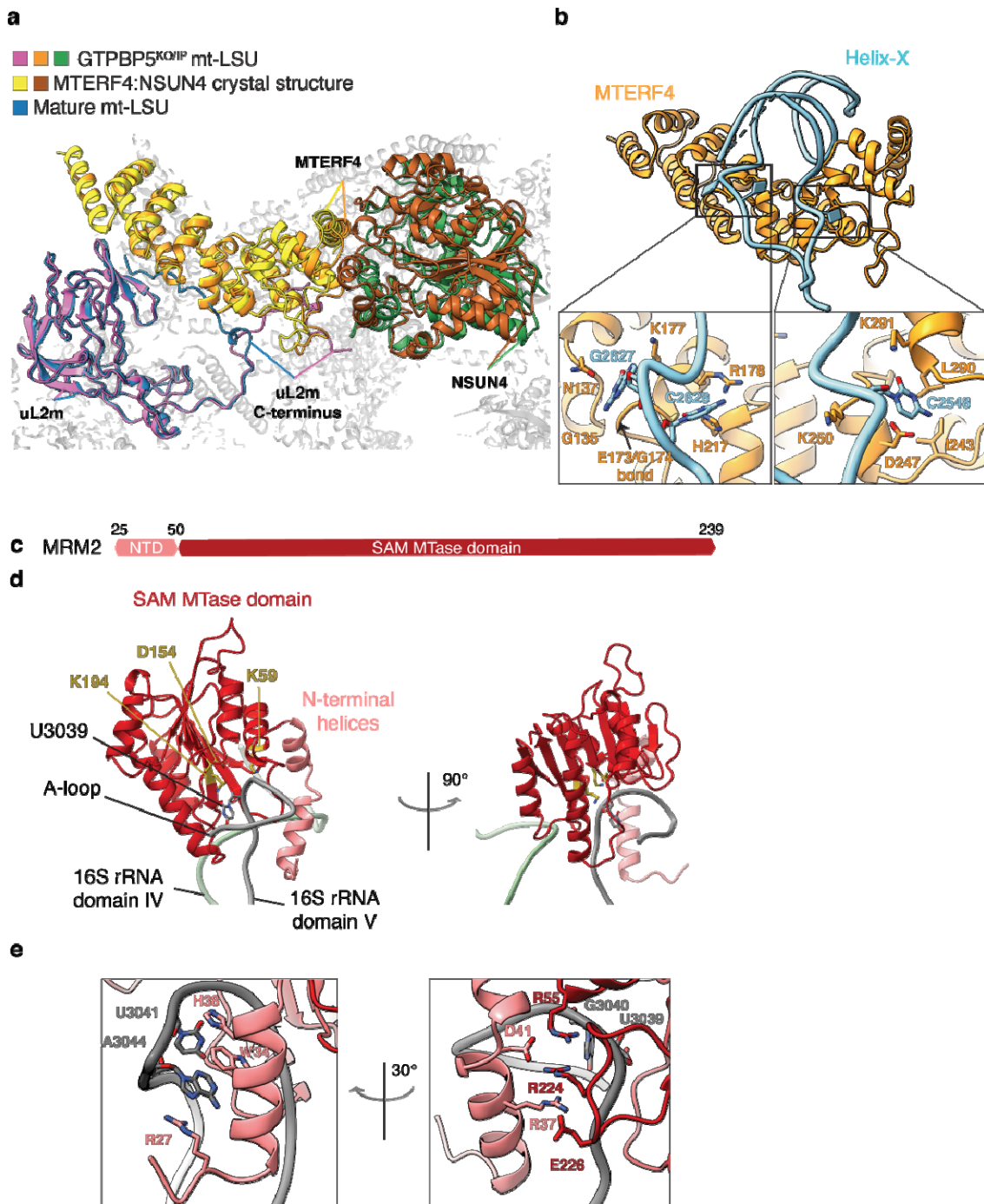
537

538

539

540

541

Fig. 2: MTERF4-NSUN4 and MRM2 interaction with the mt-LSU assembly intermediates. a, Comparison of the MTERF4-NSUN4 complex bound to the GTPBP5[KO/IP] mt-LSU (orange and green respectively) with the MTERF4-NSUN4 crystal structure (PDB: 4FP9 [18]) (yellow and brown, respectively), and of uL2m from the GTPBP5[KO/IP] mt-LSU (pink) with uL2m from the mature mt-LSU (blue) (PDB: 3J7Y [14]). The uL2m C-terminus is indicated in both structures. Helix-X is not shown. **b**, MTERF4-NSUN4 complex bound to helix-X. Zoom-in panels show the interactions of MTERF4 with helix-X. **c,** Schematic representation of MRM2 domains (NTD - light pink, SAM MTase domain - red). **d**, MRM2 interaction with the domain IV rRNA (nucleotides 2644-2652, green) and the A-loop (grey). The MRM2 methylation site (U3039) as well as the catalytic triad of MRM2 (K59,

551 D154, K194) are highlighted as sticks. **e**, Zoomed-in views showing MRM2 interactions with the A-loop in
552 different orientations.
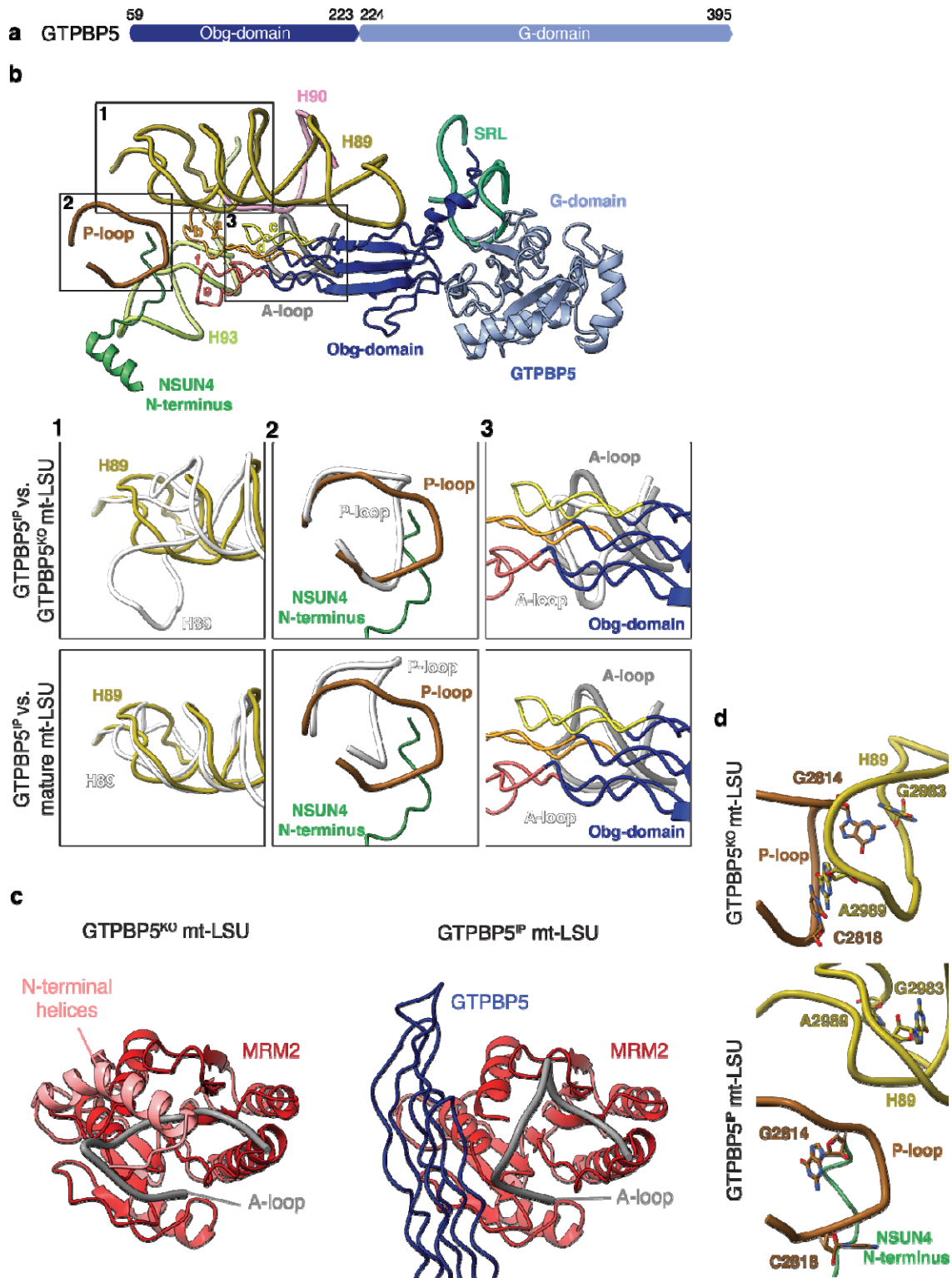
553
Fig. 3: GTPBP5 contributes to the maturation of the PTC region. a, Schematic representation of GTPBP5
555 domains (Obg-domain dark blue, G-domain light blue). **b**, Overview of GTPBP5 interactions with the 16S
556 rRNA. The Obg-domain (dark blue) contacts helices that are in the PTC region: P-loop, A-loop, H89, H90, H93.

557   Helices a-f of GTPBP5 Obg-domain are indicated. The SRL and the NSUN4 N-terminus are shown. Boxes 1-3

558   show the remodelling of the PTC in GTPBP5^{IP} mt-LSU (in color) compared with GTPBP5^{KO} mt-LSU (in white,

559   higher panel) and with the mature mt-LSU (in white, lower panel) (PDB: 6ZSG[15]). **c**, Comparison of MRM2

560   (red) and the A-loop (grey) conformations between GTPBP5^{KO} mt-LSU (left) and GTPBP5^{IP} mt-LSU (right).

561   The N-terminal helices (pink) of MRM2 could not be modelled in the GTPBP5^{IP} mt-LSU. The GTPBP5 Obg-

562   domain is shown in dark blue. **d**, Comparison of the P-loop and H89 conformations between GTPBP5^{IP} mt-LSU

563   (lower panel) and GTPBP5^{KO} mt-LSU structures (higher panel).

564

565

566

567

568

569

570

571

572

573

574

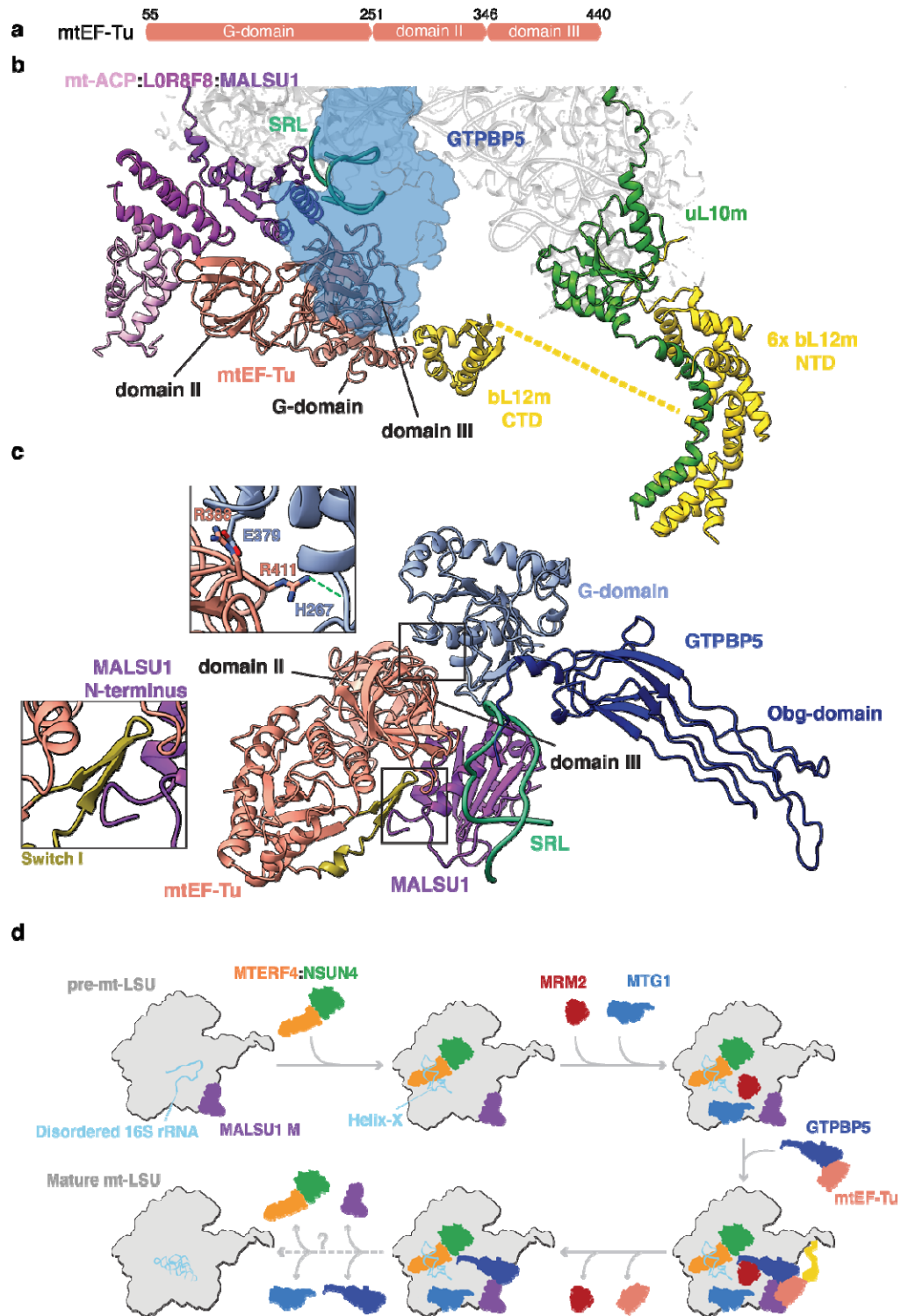575

576

577

578

579

580

581

582

21

Fig. 4: Interaction of mtEF-Tu with the mt-LSU assembly intermediate and model of the final steps of mt-LSU biogenesis. a, Schematic representation of mtEF-Tu domains. **b**, mtEF-Tu interaction with GTPBP5, the MALSU1 module and the bL12m C-terminal domain. mtEF-Tu G-domain, domain II and domain III and the SRL are indicated. The six copies of bL12m N-terminal domain and uL10m are also highlighted. The yellow

589   dashed line indicates a hypothetical connection between bL12m CTD and one of the six copies of bL12m NTD,

590   not visible in the structure. **c**, Representation of the mtEF-Tu interaction with GTPBP5 and MALSU1. The upper

591   zoomed-in panel features interactions between the GTPBP5 G-domain and the mtEF-Tu domain III. The green

592   dashed line indicates interactions to the RNA phosphate backbone. The lower zoomed-in panel shows the mtEF-

593   Tu switch I interaction with MALSU1. **d**, Final steps of the mt-LSU assembly. The dashed arrow indicates that

594   biogenesis factors are released in an unknown order.

595

596